





**Signatures of an atomic crystal in the band structure of a C<sub>60</sub> thin film**

Norman Haag,<sup>1</sup> Daniel Lüftner,<sup>2</sup> Florian Haag,<sup>1</sup> Johannes Seidel,<sup>1</sup> Leah L. Kelly ,<sup>1</sup> Giovanni Zamborini ,<sup>3,4</sup> Matteo Jugovac,<sup>4</sup> Vitaliy Feyer,<sup>4</sup> Martin Aeschlimann,<sup>1</sup> Peter Puschnig,<sup>2</sup> Mirko Cinchetti ,<sup>3</sup> and Benjamin Stadtmüller <sup>1,\*</sup>

<sup>1</sup>*Department of Physics and Research Center OPTIMAS, University of Kaiserslautern, 67663 Kaiserslautern, Germany*

<sup>2</sup>*Institute of Physics, University of Graz, NAWI Graz, Universitätsplatz 5, 8010 Graz, Austria*

<sup>3</sup>*Experimentelle Physik VI, Technische Universität Dortmund, 44221 Dortmund, Germany*

<sup>4</sup>*Peter Grünberg Institut (PGI-6), Forschungszentrum Jülich, 52425 Jülich, Germany*



(Received 10 October 2019; revised manuscript received 24 January 2020; accepted 9 March 2020; published 21 April 2020)

Transport phenomena in molecular materials are intrinsically linked to the orbital character and the degree of localization of the valence states. Here we combine angle-resolved photoemission with photoemission tomography to determine the spatial distribution of all molecular states of the valence band structure of a C<sub>60</sub> thin film. While the two most frontier valence states exhibit a strong band dispersion, the states at larger binding energies are characterized by distinct emission patterns in energy and momentum space. Our findings demonstrate the formation of an atomic crystal-like band structure in a molecular solid with delocalized  $\pi$ -like valence states and strongly localized  $\sigma$  states at larger binding energies.

DOI: [10.1103/PhysRevB.101.165422](https://doi.org/10.1103/PhysRevB.101.165422)

**I. INTRODUCTION**

In the last decades, molecular systems have emerged as highly tuneable materials for optoelectronic, photonic, and spintronic applications with the unique opportunity to actively design and control the optical band gap of light active materials by chemical functionalization [1–4]. Despite this intriguing chance for technological applications, the overall efficiency of molecular devices still suffers from the rather low charge carrier mobility and our generally poor understanding of the charge transport mechanisms in molecular solids.

These challenges have triggered intensive research focusing on both the chemical synthesis of novel molecular complexes with record charge carrier mobility [5–8] as well as the improvement of the models describing charge transport in these materials. So far it was demonstrated that charge transport in organic materials can range from purely polaron hopping transport to coherent bandlike transport depending on the band structure of the material [9–14]. While delocalization and pronounced band dispersion of the frontier orbitals, in particular, of the highest occupied molecular orbital (HOMO) and the lowest unoccupied molecular orbital (LUMO), are an important prerequisite for coherent bandlike transport, hopping transport usually occurs in molecular materials with valence states localized at the individual molecular sites. Unfortunately, even today, a quantitative understanding of the degree of delocalization of molecular transport levels for different intermolecular interactions is still elusive. This is particularly true for three-dimensional molecular complexes, such as rubrene [15,16] or the C<sub>60</sub> derivative PCBM [17], which have demonstrated exceptionally large charge carrier mobility.

In this paper we combine angle-resolved photoelectron spectroscopy (ARPES) and photoemission tomography (PT) to determine the spatial localization of all molecular orbitals of the entire valence band structure of the prototypical three-dimensional (3D) organic molecule C<sub>60</sub>. In PT, the angle-resolved photoemission yield from a molecular orbital can be interpreted as the Fourier transform of the corresponding real-space molecular wave function [18]. Despite the simplicity of this model, which roots in the assumption of a plane-wave final state, it has been extremely successful in explaining the ARPES signatures of planar  $\pi$ -conjugated molecules adsorbed on surfaces [19–26] and to disentangle the spectroscopic signatures of structural or chemically inequivalent planar molecules in monolayer films on surfaces [23,27,28]. Only very recently, the plane-wave final state was also applied to predict the ARPES signatures of a monolayer film of nonplanar fullerene molecules on a metal surface [29].

Here we focus on the band structure of a thin C<sub>60</sub> film on the Ag(111) surface. We find that the two most frontier molecular orbitals reveal a strong band dispersion while the energetically lower lying orbitals appear as distinct emission maxima in energy and momentum space. These differences can be explained by density functional theory (DFT) calculations of a free-standing C<sub>60</sub> layer in conjunction with PT simulations. Accordingly, we can assign the strongly dispersing bands to the HOMO and HOMO-1 with pure  $\pi$ -orbital character which spread over adjacent molecules. In contrast, the sharper emission maxima at larger binding energies are caused by  $\sigma$  orbitals that are localized on the individual C<sub>60</sub> sites. Our findings demonstrate that the band structure of molecular materials can exhibit the same characteristic signatures known from any crystalline inorganic material with delocalized valence and localized (molecular) core level states.

\*bstadtmueller@physik.uni-kl.de

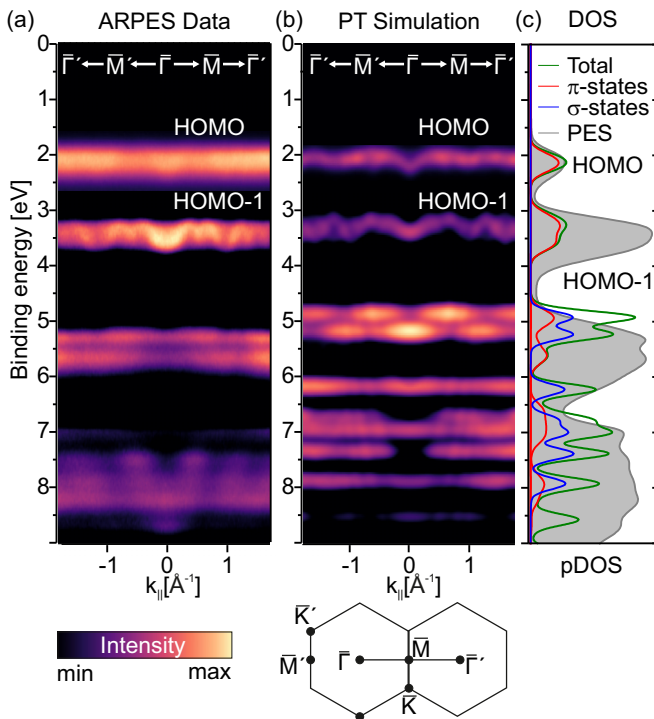


FIG. 1. (a) Energy vs momentum cut through the ARPES data along the  $\bar{\Gamma} \bar{M} \bar{\Gamma}'$  direction of the surface Brillouin zone for a crystalline  $C_{60}$  thin film (5 ML,  $E_{\text{photon}} = 35$  eV,  $p$ -polarized light). The surface Brillouin zone is shown in the lower panel together with the intensity scale of the ARPES data. (b) PT simulation of the same energy vs momentum cut based on a DFT calculation of a free-standing  $C_{60}$  layer. (c) Density of states projected onto the  $\pi$  and  $\sigma$  states of  $C_{60}$ . For comparison, the spectral density of the total photoemission yield is included as a gray curve.

## II. RESULTS AND DISCUSSION

We start with an overview of the molecular band structure of the  $C_{60}$  thin film (5 ML) on Ag(111). The  $C_{60}$  molecules arrange in a crystalline  $(2\sqrt{3} \times 2\sqrt{3})R30^\circ$  structure with two coexisting structural domains which are rotated by  $\pm 18^\circ$ . To suppress any thermally induced rotation of the  $C_{60}$  molecules, the sample temperature was kept below 150 K throughout the experiment [30]. At this low temperature, molecular motion is suppressed and the  $C_{60}$  crystal undergoes a phase transition into a simple cubic phase with four  $C_{60}$  molecules per surface unit cell: one hexagon prone and three double-bond prone molecules [31,32]. All photoemission data were acquired with a momentum microscope and synchrotron radiation at the Elettra Synchrotron Light Source, which allows us to record the complete energy and momentum dependent photoemission yield within the photoemission horizon in a fixed experimental geometry [33,34]. More details can be found in the Supplemental Material [35] (see, also, Refs. [36,37] therein).

Figure 1(a) shows the molecular valence band structure of the  $C_{60}$  film as an energy vs momentum cut along the  $\bar{\Gamma} \bar{M} \bar{\Gamma}'$  direction of the surface Brillouin zone of the  $C_{60}$  crystal. We find significant differences in the energy and momentum distributions of the molecular features depending on their

binding energy. The first two molecular states ( $E_B < 5$  eV) show a band dispersion (bandwidth) of up to 700 meV. This bandwidth is rather large for molecular materials with predominant van der Waals interactions, but still smaller compared to the typical bandwidth of inorganic semiconductors or other inorganic crystalline materials [38,39]. In contrast, the molecular features at larger binding energies ( $E_B > 5$  eV) appear as distinct maxima in energy and momentum space. Therefore, at first glance, the band structure of the  $C_{60}$  film reveals all characteristic features of the band structure of an atomic solid with dispersing valence bands and localized (molecular) core level states.

Theoretical insight into the ARPES data can be obtained by the PT simulation based on DFT calculations [40] of a free-standing  $C_{60}$  layer with four molecules per unit cell (details can be found in the Supplemental Material [35], and Refs. [41–44] therein). We calculated the 3D Fourier transform of the molecular wave function of each molecular state and extracted the photoemission signal by a spherical cut through the 3D Fourier transform in momentum space [18], an approach which has recently been extended to account for two-dimensional (2D) dispersion layers [45]. The radius of the spherical momentum space cut is determined by the total momentum  $k_{\text{final}}$  of the electrons in the photoemission final state. For planar molecules on surfaces,  $k_{\text{final}}$  is determined by the kinetic energy of the emitted photoelectrons. In case of our  $C_{60}$  film, we additionally need to consider the inner potential  $V_0$  which renormalizes the perpendicular component  $k_z$  of the electron momentum in the final state. This is particularly crucial for 3D molecules for which the 3D Fourier transform reveals a strong intensity modulation along the  $k_z$  direction (see also Fig. 6 in the Supplemental Material [35]).

For the PT simulation we used the inner potential of  $V_0 = 13$  eV, which was determined experimentally by Hasegawa *et al.* [46]. The corresponding energy vs momentum cut of our PT simulations along the  $\bar{\Gamma} \bar{M} \bar{\Gamma}'$  direction is shown in Fig. 1(b). Note that we have aligned the energy of the topmost band with its experimentally observed binding energy position. We find an excellent agreement between the PT simulation and the experimental data [Fig. 1(a)]. The PT simulation reveals two dispersing bands for small binding energies with a comparable bandwidth and energy difference as observed experimentally, and discrete emission features for binding energies larger than  $E_B > 5$  eV. The almost rigid energy shift of the lower-lying states in the simulation with respect to the experiment is typical for the used generalized gradient approximation (GGA) functional [47] and can be attributed to self-interaction errors.

The overall excellent agreement between experiment and theory allows us to determine the orbital character of all molecular photoemission signatures by projecting the density of states onto the  $\pi$  and  $\sigma$  orbitals of  $C_{60}$ . The corresponding projected density of states (pDOS) is shown in Fig. 1(c). The pDOS of the two most frontier orbitals is purely dominated by  $\pi$  states and can hence be attributed to the HOMO and HOMO-1 bands of  $C_{60}$ . Importantly, the HOMO band is derived from the five  $H_u$  orbitals, the HOMO-1 from the four  $G_g$  and five  $H_g$  orbitals of the free  $C_{60}$  molecule. At larger binding energy, the molecular photoemission signals contain a mixture of  $\pi$  and  $\sigma$  states.

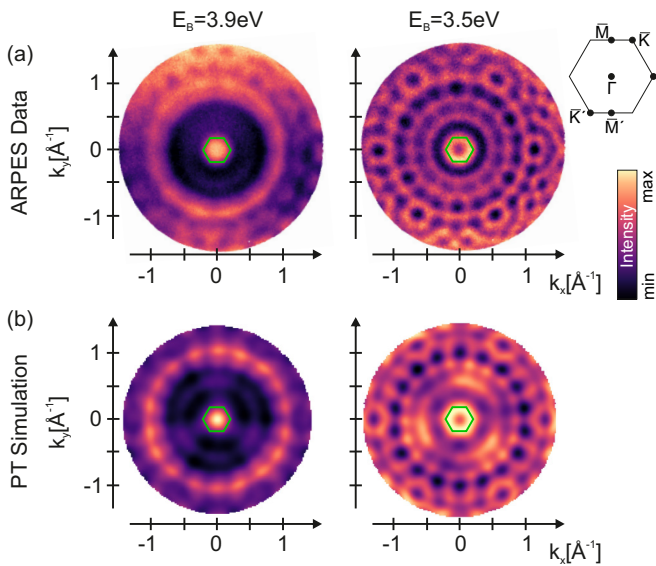


FIG. 2. (a) Constant energy (CE) maps extracted from the ARPES data cube in the binding energy region of the HOMO-1 band at  $E_B = 2.9$  eV and  $E_B = 3.5$  eV. The corresponding CE maps predicted by our photoemission tomography simulation (PT) are shown in (b) for identical binding energies.

The predictive power of our PT simulations becomes even clearer when turning to the constant energy (CE) momentum maps, which show the momentum-resolved photoemission yield in the entire accessible momentum space range at a constant energy. These CE maps are the typical representation of the PT simulations since they directly reflect the periodicity of the molecular wave functions in real space.

Figure 2(a) shows CE maps extracted at two characteristic binding energies within the HOMO-1 band. The green hexagon marks the surface Brillouin zone of the  $C_{60}$  crystal structure. All CE maps exhibit a quite complex momentum space pattern with sharp maxima which change their position and shape when scanning through the binding energy. For instance, the feature in the center of the surface Brillouin zone transforms from a dotlike emission at  $E_B = 3.9$  eV into a ringlike emission at  $E_B = 3.5$  eV. This is clearly the spectroscopic signature of an upwards dispersing band in agreement with the energy vs momentum cut in Fig. 1(a). The emission features at larger momentum can be attributed to the same state repeated in the second and third Brillouin zones.

The PT simulations at the corresponding binding energies within the HOMO-1 band are shown in Fig. 2(b). These maps were obtained by considering the spectroscopic signatures of the main  $(2\sqrt{3} \times 2\sqrt{3})R30^\circ$  structure as well as of the co-existing rotational domains as discussed in the Supplemental Material [35]. The agreement between the PT simulations and our experimental data is striking and hence further confirms our previous assignment of the strongly dispersing bands to molecular orbitals with  $\pi$ -orbital character.

To go beyond a pure qualitative analysis, we now focus on the band dispersion of the HOMO and HOMO-1 bands. The band dispersions of the HOMO-1 band were recorded with vertical ( $p$ ) and horizontal ( $s$ ) polarization of the synchrotron radiation (angle of incidence:  $65^\circ$  with respect to the surface

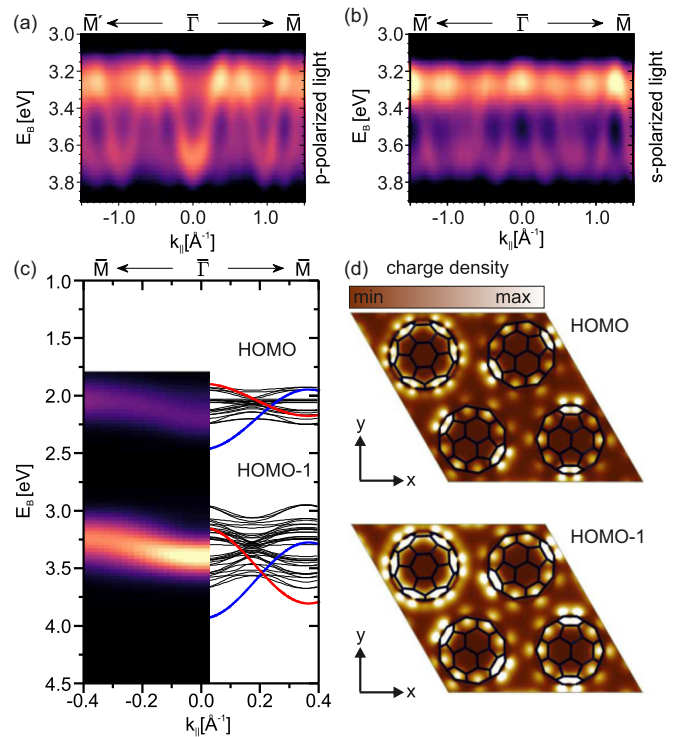


FIG. 3. Energy vs momentum cut of the HOMO-1 bands of a  $C_{60}$  thin film recorded with vertical (a) and horizontal (b) light polarization ( $E_{\text{photon}} = 35$  eV). The contrast of both energy vs momentum cuts is enhanced by using the second derivative of the experimental data. The left half of (c) shows the PT simulation of the energy vs momentum cut in the first Brillouin zone, the right half the band structure of our density functional theory calculation. The red and blue solid lines are tight-binding simulations to describe the experimental band dispersion observed for  $p$ - (blue) and  $s$ -polarized light (red). (d) Real-space partial charge density distributions of the HOMO and HOMO-1 bands integrated in energy windows from 1.5 to 2.5 eV and 2.75 to 4.0 eV for the HOMO and HOMO-1 respectively. The partial charge density plots are shown in a top view of the  $C_{60}$  unit cell in a plane through the center of the  $C_{60}$  molecules.

normal). The corresponding energy vs momentum cuts are displayed in Figs. 3(a) and 3(b), respectively. Both band dispersions exhibit clear qualitative differences depending on the light polarization. For  $p$ -polarized light, the HOMO-1 band at the  $\Gamma$  point disperses upward while it disperses downward for  $s$ -polarized light. This qualitative difference in the ARPES data obtained with  $p$ - and  $s$ -polarized light demonstrates the existence of at least two bands with different orbital character in the binding energy range of the HOMO-1 state. Similar results were also observed for the HOMO band.

For the quantification of the band dispersion, we extracted the diameter of the almost ringlike band in the first surface Brillouin zone for all CE maps of the HOMO and HOMO-1 bands. For each orbital, we observe two bands, one with positive effective band mass (upwards dispersing band) and one with negative effective band mass (downwards dispersing band). The bands with positive effective mass are observed with  $p$ -polarized light suggesting a strong contribution of  $p_z$  orbitals of the  $C_{60}$  thin film. In contrast, the bands with negative band mass are dominated by  $\pi$  orbitals with a strong



in-plane orbital character, i.e., with  $p_{x/y}$  orbitals character. The band dispersion is further analyzed by a tight-binding model calculated for a 2D hexagonal lattice [48] which are shown in the right half of Fig. 3(c) as red and blue solid curves. The effective masses of the HOMO-1 bands are  $\pm 5 m_0$ , while the ones of the HOMO bands are 6 and  $-10 m_0$ , respectively. These band masses correspond to an oscillation bandwidth of 0.28–0.66 eV, in good agreement with previous studies of  $C_{60}$  [14,49–51].

The PT simulation of the band dispersion of the HOMO and HOMO-1 in the first surface Brillouin zone is shown in the left half of Fig. 3(c). In contrast to our photoemission data, we only find one band with positive effective band mass, which is in qualitative agreement with our experimental findings obtained with  $p$ -polarized light. At this point, it is important to note that for the PT simulation, a plane-wave final state has been assumed. This approximation is known to work well for experimental geometries where the emission direction is close to parallel to the light polarization [18] corresponding to  $p$  polarization in our case. Although the PT simulation can presently not account for the difference between  $p$  and  $s$  polarization, it clearly goes beyond a mere DFT band structure calculation. This is illustrated in the right half of Fig. 3(c), which depicts all bands calculated with DFT for the unit cell containing four  $C_{60}$  molecules:  $4 \times 5 = 20$  bands for the HOMO and  $4 \times 9 = 36$  bands for the HOMO-1. Here we observe both bands of positive and negative band mass in the binding energy range of the HOMO and HOMO-1 level, in agreement with a recent band structure calculation of a free-standing  $C_{60}$  layer [14]. By taking into account the photoemission cross sections, as is done in the PT simulation, only certain bands get selected which allows for a more realistic comparison with experimental ARPES data.

The large dispersion of the HOMO and HOMO-1 bands can also be understood by plotting the partial charge density distributions in Fig. 3(d) in a top view of the  $C_{60}$  unit cell in a plane through the center of the  $C_{60}$  molecules. For both orbitals, the charge density is not only localized on the molecular carbon cage but also in the free space between the fullerenes. The latter points to a significant overlap of the frontier molecular  $\pi$  orbitals of neighboring molecules in the thin film which is hence responsible for the large band dispersion of the HOMO and HOMO-1 band of  $C_{60}$ .

We now focus on the molecular states which can be found for  $E_B > 5$  eV. The photoemission signals in this binding energy range are dominated by  $\sigma$  states with discrete maxima in the energy vs momentum space. Interestingly, these discrete maxima are not randomly distributed in energy and momentum space but are all arranged along lines, see Fig. 1(a). This observation is also directly reflected in the CE maps in Fig. 4(a) which were extracted at 8.7, 7.9, and 7.4 eV. They consist of ringlike intensity distributions with energy dependent radii which increase for smaller binding energies. Such a distinct correlation can be attributed to an intramolecular band dispersion of the molecular  $\sigma$  states as observed by Koller *et al.* for crystalline films of sexiphenyl molecules [52]. The absence of a significant intermolecular dispersion of these bands can be understood by their  $\sigma$  character which leads to a negligible intermolecular overlap of wave functions for adjacent molecules.

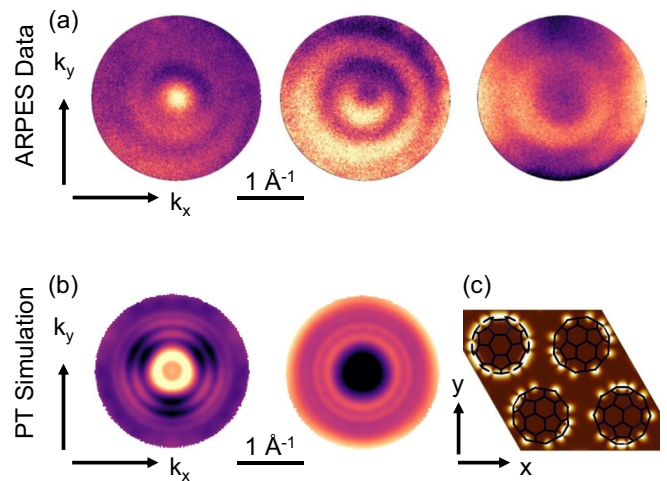


FIG. 4. (a) Experimentally determined CE maps at three selected energies from left to right: 8.7, 7.9, and 7.4 eV. The corresponding PT simulations are shown in (b). Note that the CE maps in the PT simulations were extracted at slightly different binding energies as the experimental data. This is due to an energy difference in the initial state energy in our experiment and in the DFT calculations. (c) Partial charge density in real space of a  $\sigma$  state integrated in energy windows from 6.0 to 6.5 eV.

Our experimental findings are qualitatively well reproduced by PT simulations. In particular, the simulated CE maps exhibit concentric emission features with increasing radius for smaller binding energies, see Fig. 4(b). The overall emission pattern agrees qualitatively with our ARPES data and enables us to gain insight into the spatial structure of the molecular orbitals in real space with high confidence. The spatial charge density distribution in Fig. 4(c) was integrated from 6.0 to 6.5 eV. We find that the entire charge density is localized on the carbon cage of all four molecules of the unit cell while no charge density can be observed between the  $C_{60}$  molecules. This clearly points to the absence of any overlap of the molecular wave functions for  $\sigma$  states which explains the absence of intermolecular dispersion of these orbitals at large binding energies.

Minor quantitative deviations between the ARPES data and the PT simulations can be attributed to the different initial state energy of the  $\sigma$  states in the experiment and the band structure calculation in conjunction with the strong  $k_z$  dependency of the 3D Fourier transform of the localized molecular states of nonplanar molecules. Both aspects are discussed in more detail in the Supplemental Material [35].

### III. CONCLUSION

In conclusion, we have provided insights into the band dispersion and spatial delocalization of molecular orbitals of the prototypical three-dimensional molecule  $C_{60}$ . Our photoemission experiment reveals two strongly dispersing molecular states with complex momentum-dependent photoemission patterns for small binding energies and nondispersing emission maxima in energy and momentum space for larger binding energies. These different momentum-dependent photoemission distributions can be qualitatively described by our

photoemission tomography simulations considering a plane-wave final state, the inner potential of the  $C_{60}$  thin film, and the band structure of a free-standing  $C_{60}$  layer. This further confirms the applicability of PT to ARPES data of nonplanar, three-dimensional molecular complexes [29]. Even more importantly, it allows us to assign the strongly dispersing bands to molecular states with pure  $\pi$ -orbital character that are delocalized over neighboring molecular sites and the nondispersing emission pattern to localized  $\sigma$  states of the individual  $C_{60}$  molecules.

In this way we were able to demonstrate the formation of an atomic crystal-like band structure in a molecular thin film. This is an important step towards a better understanding of charge carrier transport in thin films of chemically designed molecules with superior functionalities, which, in most cases, exhibit a nonplanar molecular structure.

## ACKNOWLEDGMENTS

The work was funded by the Deutsche Forschungsgemeinschaft (DFG, German Research Foundation) - TRR 173 - 268565370 (Project B05). B.S. and F.H. thankfully acknowledge financial support from the Graduate School of Excellence MAINZ (Excellence Initiative DFG/GSC 266). L.L.K. acknowledges financial support from Carl-Zeiss Stiftung for post-doctoral fellowship. M.C. and G.Z. acknowledge funding from the European Research Council (ERC) under the European Union's Horizon 2020 research and innovation programme (Grant Agreement No. 725767 - hyControl). D.L. and P.P. acknowledge support from the Austrian Science Fund (FWF) through Project I3731. The computations have been performed on the HPC cluster of the KFU Graz and at the Vienna Scientific Computer (VSC). We acknowledge Elettra for providing the synchrotron radiation facility.

- 
- [1] M. Schwarze, W. Tress, B. Beyer, F. Gao, R. Scholz, C. Poelking, K. Ortstein, A. A. Günther, D. Kasemann, D. Andrienko *et al.*, *Science* **352**, 1446 (2016).
- [2] C. Bizzarri, E. Spuling, D. M. Knoll, D. Volz, and S. Bräse, *Coord. Chem. Rev.* **373**, 49 (2018).
- [3] H. Xu, R. Chen, Q. Sun, W. Lai, Q. Su, W. Huang, and X. Liu, *Chem. Soc. Rev.* **43**, 3259 (2014).
- [4] M. Cinchetti, V. A. Dediu, and L. E. Hueso, *Nat. Mater.* **16**, 507 (2017).
- [5] J. E. Anthony, *Chem. Rev.* **106**, 5028 (2006).
- [6] C. Wang, H. Dong, W. Hu, Y. Liu, and D. Zhu, *Chem. Rev.* **112**, 2208 (2012).
- [7] I. Kang, H.-J. Yun, D. S. Chung, S.-K. Kwon, and Y.-H. Kim, *J. Am. Chem. Soc.* **135**, 14896 (2013).
- [8] J. Liu, H. Zhang, H. Dong, L. Meng, L. Jiang, L. Jiang, Y. Wang, J. Yu, Y. Sun, W. Hu *et al.*, *Nat. Commun.* **6**, 10032 (2015).
- [9] N. Ueno and S. Kera, *Prog. Surf. Sci.* **83**, 490 (2008).
- [10] J.-L. Brédas, D. Beljonne, V. Coropceanu, and J. Cornil, *Chem. Rev.* **104**, 4971 (2004).
- [11] S. Kera and N. Ueno, *J. Electron. Spectrosc. Relat. Phenom.* **204**, 2 (2015).
- [12] S.-i. Machida, Y. Nakayama, S. Duhm, Q. Xin, A. Funakoshi, N. Ogawa, S. Kera, N. Ueno, and H. Ishii, *Phys. Rev. Lett.* **104**, 156401 (2010).
- [13] F. Bussolotti, J. Yang, T. Yamaguchi, K. Yonezawa, K. Sato, M. Matsunami, K. Tanaka, Y. Nakayama, H. Ishii, N. Ueno *et al.*, *Nat. Commun.* **8**, 173 (2017).
- [14] D. W. Latzke, C. Ojeda-Aristizabal, S. M. Griffin, J. D. Denlinger, J. B. Neaton, A. Zettl, and A. Lanzara, *Phys. Rev. B* **99**, 045425 (2019).
- [15] E. Menard, V. Podzorov, S.-H. Hur, A. Gaur, M. E. Gershenson, and J. A. Rogers, *Adv. Mater.* **16**, 2097 (2004).
- [16] V. C. Sundar, J. Zaumseil, V. Podzorov, E. Menard, R. L. Willett, T. Someya, M. E. Gershenson, and J. A. Rogers, *Science* **303**, 1644 (2004).
- [17] T. D. Anthopoulos, C. Tanase, S. Setayesh, E. J. Meijer, J. C. Hummelen, P. W. M. Blom, and D. M. de Leeuw, *Adv. Mater.* **16**, 2174 (2004).
- [18] P. Puschnig, S. Berkebile, A. J. Fleming, G. Koller, K. Emtsev, T. Seyller, J. D. Riley, C. Ambrosch-Draxl, F. P. Netzer, and M. G. Ramsey, *Science* **326**, 702 (2009).
- [19] J. Ziroff, F. Forster, A. Schöll, P. Puschnig, and F. Reinert, *Phys. Rev. Lett.* **104**, 233004 (2010).
- [20] M. Willenböckel, B. Stadtmüller, K. Schönauer, F. C. Bocquet, D. Lüftner, E. M. Reinisch, T. Ules, G. Koller, C. Kumpf, S. Soubatch *et al.*, *New J. Phys.* **15**, 033017 (2013).
- [21] V. Feyer, M. Graus, P. Nigge, M. Wießner, R. G. Acres, C. Wiemann, C. M. Schneider, A. Schöll, and F. Reinert, *Surf. Sci.* **621**, 64 (2014).
- [22] M. Grimm, C. Metzger, M. Graus, M. Jugovac, G. Zamborlini, V. Feyer, A. Schöll, and F. Reinert, *Phys. Rev. B* **98**, 195412 (2018).
- [23] B. Stadtmüller, M. Willenböckel, E. M. Reinisch, T. Ules, F. C. Bocquet, S. Soubatch, P. Puschnig, G. Koller, M. G. Ramsey, F. S. Tautz *et al.*, *Europhys. Lett.* **100**, 26008 (2012).
- [24] S. Weiss, D. Luftner, T. Ules, E. M. Reinisch, H. Kaser, A. Gottwald, M. Richter, S. Soubatch, G. Koller, M. G. Ramsey *et al.*, *Nat. Commun.* **6**, 8287 (2015).
- [25] L. Egger, B. Kollmann, P. Hurdax, D. Lüftner, X. Yang, S. Weiss, A. Gottwald, M. Richter, G. Koller, S. Soubatch *et al.*, *New J. Phys.* **21**, 043003 (2019).
- [26] G. Zamborlini, D. Lüftner, Z. Feng, B. Kollmann, P. Puschnig, C. Dri, M. Panighel, G. Di Santo, A. Goldoni, G. Comelli *et al.*, *Nat. Commun.* **8**, 335 (2017).
- [27] B. Stadtmüller, D. Lüftner, M. Willenböckel, E. M. Reinisch, T. Sueyoshi, G. Koller, S. Soubatch, M. G. Ramsey, P. Puschnig, F. S. Tautz *et al.*, *Nat. Commun.* **5**, 3685 (2014).
- [28] M. Willenböckel, D. Lüftner, B. Stadtmüller, G. Koller, C. Kumpf, S. Soubatch, P. Puschnig, M. G. Ramsey, and F. S. Tautz, *Phys. Chem. Chem. Phys.* **17**, 1530 (2015).
- [29] C. Metzger, M. Graus, M. Grimm, G. Zamborlini, V. Feyer, M. Schwendt, D. Lüftner, P. Puschnig, A. Schöll, and F. Reinert *Phys. Rev. B* **101**, 165421 (2020).
- [30] M. S. Dresselhaus, G. Dresselhaus, and P. C. Eklund, *Science of Fullerenes and Carbon Nanotubes: Their Properties and Applications*, 1st ed. (Elsevier, Amsterdam, 1996).

- [31] W. I. F. David, R. M. Ibberson, T. J. S. Dennis, J. P. Hare, and K. Prassides, *Europhys. Lett.* **18**, 219 (1992).
- [32] W. I. F. David, R. M. Ibberson, J. C. Matthewman, K. Prassides, T. J. S. Dennis, J. P. Hare, H. W. Kroto, R. Taylor, and D. R. M. Walton, *Nature (London)* **353**, 147 (1991).
- [33] B. Krömker, M. Escher, D. Funnemann, D. Hartung, H. Engelhard, and J. Kirschner, *Rev. Sci. Instrum.* **79**, 053702 (2008).
- [34] C. Tusche, M. Ellguth, A. Krasnyuk, A. Winkelmann, D. Kutnyakhov, P. Lushchyk, K. Medjanik, G. Schonhense, and J. Kirschner, *Ultramicroscopy* **130**, 70 (2013).
- [35] See Supplemental Material at <http://link.aps.org/supplemental/10.1103/PhysRevB.101.165422> for more information about the sample preparation procedure, the crystal structure of the C<sub>60</sub> thin films, as well as the experimental and theoretical methods. In addition, we provide information regarding the photoemission tomography approach for three-dimensional molecular complexes.
- [36] X.-Q. Shi, M. A. van Hove, and R.-Q. Zhang, *J. Mater. Sci.* **47**, 7341 (2012).
- [37] A. Tamai, A. P. Seitsonen, R. Fasel, Z.-X. Shen, J. Osterwalder, and T. Greber, *Phys. Rev. B* **72**, 085421 (2005).
- [38] R. Hoffmann, *Angew. Chem.* **26**, 846 (1987).
- [39] D. Golze, M. Dvorak, and P. Rinke, *Front. Chem.* **7**, 377 (2019).
- [40] J. P. Perdew, K. Burke, and M. Ernzerhof, *Phys. Rev. Lett.* **77**, 3865 (1996).
- [41] G. Kresse and J. Hafner, *Phys. Rev. B* **47**, 558 (1993).
- [42] G. Kresse and D. Joubert, *Phys. Rev. B* **59**, 1758 (1999).
- [43] A. Tkatchenko and M. Scheffler, *Phys. Rev. Lett.* **102**, 073005 (2009).
- [44] P. E. Blöchl, *Phys. Rev. B* **50**, 17953 (1994).
- [45] D. Lüftner, S. Weiß, X. Yang, P. Hurdax, V. Feyer, A. Gottwald, G. Koller, S. Soubatch, P. Puschnig, M. G. Ramsey *et al.*, *Phys. Rev. B* **96**, 125402 (2017).
- [46] S. Hasegawa, T. Miyamae, K. Yakushi, H. Inokuchi, K. Seki, and N. Ueno, *Phys. Rev. B* **58**, 4927 (1998).
- [47] P. Puschnig and D. Lüftner, *J. Electron. Spectrosc. Relat. Phenom.* **200**, 193 (2015).
- [48] X.-Y. Zhu, G. Dutton, D. P. Quinn, C. D. Lindstrom, N. E. Schultz, and D. G. Truhlar, *Phys. Rev. B* **74**, 241401(R) (2006).
- [49] A. Tamai, A. P. Seitsonen, T. Greber, and J. Osterwalder, *Phys. Rev. B* **74**, 085407 (2006).
- [50] S. He, M. Arita, H. Namatame, M. Taniguchi, H.-N. Li, and H.-Y. Li, *J. Phys. Condens. Matter* **19**, 026202 (2006).
- [51] B. Stadtmüller, S. Emmerich, D. Jungkenn, N. Haag, M. Rollinger, S. Eich, M. Maniraj, M. Aeschlimann, M. Cinchetti, and S. Mathias, *Nat. Commun.* **10**, 1470 (2019).
- [52] G. Koller, S. Berkebile, M. Oehzelt, P. Puschnig, C. Ambrosch-Draxl, F. P. Netzer, and M. G. Ramsey, *Science* **317**, 351 (2007).